Astronomy & Astrophysics

J0526+5934: A peculiar ultra-short-period double white dwarf

Alberto Rebassa-Mansergas[1,2], Mark Hollands[3], Steven G. Parsons[3], Leandro G. Althaus[4,5], Ingrid Pelisoli[6],
Puji Irawati[7] , Roberto Raddi[1], Maria E. Camisassa[1], and Santiago Torres[1,2]

[1] Departament de Física, Universitat Politècnica de Catalunya, c/Esteve Terrades 5, 08860 Castelldefels, Spain
e-mail: alberto.rebassa@upc.edu
[2] Institute for Space Studies of Catalonia (IEEC), c/Esteve Terradas,1, Edifici RDIT, Despatx 212, Campus del Baix Llobregat UPC
– Parc Mediterrani de la Tecnologia, 08860 Castelldefels, Spain
[3] Department of Physics and Astronomy, University of Sheffield, Sheffield S3 7RH, UK
[4] Facultad de Ciencias Astronómicas y Geofísicas, Universidad Nacional de La Plata, Paseo del Bosque s/n, 1900 La Plata, Argentina
[5] Instituto de Astrofísica La Plata, UNLP-CONICET, Paseo del Bosque s/n, 1900 La Plata, Argentina
[6] Department of Physics, University of Warwick, Coventry CV4 7AL, UK
[7] National Astronomical Research Institute of Thailand, 260 Moo 4, T. Donkaew, A. Maerim, Chiangmai 50180, Thailand

Received 6 February 2024 / Accepted 8 April 2024

ABSTRACT

Context. Ultra-short-period compact binaries are important sources of gravitational waves. The class of short-period compact binaries includes, for example, the progenitors of type Ia supernovae and the progenitors of merger episodes that may lead to massive and magnetic single white dwarfs. J0526+5934 is one such example: it is an unresolved compact binary star with an orbital period of 20.5 min.
Aims. The visible component of J0526+5934 was recently claimed to be a hot sub-dwarf star with a CO white dwarf companion. Our aim is to provide strong observational and theoretical evidence that the primary star is instead an extremely low-mass white dwarf, although the hot sub-dwarf nature cannot be completely ruled out.
Methods. We analysed optical spectra together with time-series photometry of the visible component of J0526+5934 to constrain its orbital and stellar parameters. We also employed evolutionary sequences for low-mass white dwarfs to derive independent values of the primary mass.
Results. From the analysis of our observational data, we find a stellar mass for the primary star in J0526+5934 of $0.26 \pm 0.05 \, M_\odot$, which perfectly matches the $0.237 \pm 0.035 \, M_\odot$ independent measurement we derive from the theoretical evolutionary models. This value is considerably lower than the theoretically expected and generally observed mass range for hot sub-dwarf stars, but falls well within the mass limit values of extremely low-mass white dwarfs.
Conclusions. We conclude J0526+5934 is the sixth ultra-short-period detached double white dwarf currently known.

Key words. binaries: close – white dwarfs

1. Introduction

Together with low-mass main sequence stars, white dwarfs are the most common objects in our Galaxy. Indeed, over 95% of main sequence stars will become, or have already turned into, white dwarfs (Althaus et al. 2010). After all nuclear evolutionary phases take place, only the hot Earth-sized core of the star remains, typically with a mass of $\simeq 0.6 \, M_\odot$ (Hollands et al. 2018; Kilic et al. 2020; McCleery et al. 2020; Jiménez-Esteban et al. 2023; O'Brien et al. 2024). Once they are formed, these compact objects cool over periods of time longer than the Hubble time, a cooling process that is relatively well understood (Blouin et al. 2019; Bauer et al. 2020; Camisassa et al. 2016, 2019, 2023). As a consequence, white dwarfs are highly valuable tools that can be used as cosmo-chronometers to, for example, place constraints on the ages of open and globular clusters (e.g. García-Berro et al. 2010; Jeffery et al. 2011; Torres et al. 2015) and on the age of the Galactic disk (e.g. Garcia-Berro et al. 1988; Oswalt et al. 1996) and halo (e.g. Kilic et al. 2020; Torres et al. 2021). If white dwarfs are in wide enough binary systems with main sequence companions (and no mass transfer episodes took place in the past), they can be used to provide ages for their companions to thus constrain, for example, the age–metallicity relation (Rebassa-Mansergas et al. 2016, 2021) and the age–velocity

dispersion relation (Raddi et al. 2022) of the Milky Way, or the age–activity–rotation relation of low-mass main sequence stars (Rebassa-Mansergas et al. 2013, 2023; Morgan et al. 2012; Skinner et al. 2017).

White dwarf binaries are also of extreme interest when the orbital separations are short, of the order of a few days or less. In these cases, the systems most likely formed via at least one common-envelope evolution (Webbink et al. 2008). For example, post-common-envelope white dwarf–main sequence binaries have been valuable for constraining current theories of common-envelope evolution (Camacho et al. 2014; Cojocaru et al. 2017; Zorotovic & Schreiber 2022) and magnetic braking (Schreiber et al. 2010; Zorotovic et al. 2016), as well as for constraining the mass–radius relation of white dwarfs (Parsons et al. 2017), brown dwarfs (van Roestel et al. 2021), sub-dwarf stars (Rebassa-Mansergas et al. 2019a), and main sequence stars (Parsons et al. 2018) if they are eclipsing. One of the possible products of post-common-envelope systems are double white dwarfs: the main sequence companions have had time to evolve out of the main sequence, thus forcing the systems to enter a second common-envelope phase. However, it is not clear yet whether or not double white dwarfs form through two common-envelope episodes (Nelemans & Tout 2005; van der Sluys et al. 2006),
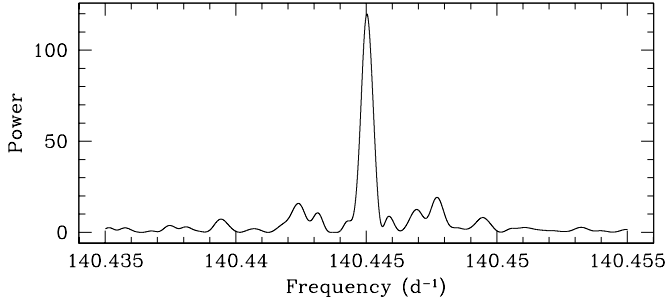
Fig. 1. Scargle periodogram of J0526+5934 resulting from our analysis of the ZTF g-band data. The strongest peak corresponds to a period of $\simeq 10$ min, which is half the true orbital period. The same result is obtained from the r-band ZTF data.

and an alternative scenario has been proposed that involves a first phase of stable but non-conservative mass transfer followed by a common-envelope episode (Woods et al. 2012; Ge et al. 2015; Schreiber et al. 2022). In any case, short-period double white dwarfs are important gravitational wave sources. They will be the dominant sources for the forthcoming Laser Interferometer Space Antenna (LISA) mission (Korol et al. 2018) and are one of the favoured systems for producing type Ia supernovae (Whelan & Iben 1973; Iben 1984; Liu et al. 2018). Finding potential double-degenerate type Ia supernova progenitors via optical spectroscopy is extremely challenging; however, they are expected to be found through detection of their gravitational waves (Rebassa-Mansergas et al. 2019b).

Currently, there are several hundred double white dwarfs known (Rebassa-Mansergas et al. 2017; Breedt et al. 2017; Maoz et al. 2018; Napiwotzki et al. 2020), many of which are eclipsing (Hallakoun et al. 2016; Parsons et al. 2020; Keller et al. 2022; Kosakowski et al. 2022; Munday et al. 2023). Of particular interest are those that contain an extremely low-mass (ELM) white dwarf ($\lesssim 0.3\,M_\odot$). These objects cannot be formed in isolated evolution, and are believed to be formed as a result of a common-envelope phase or after an episode of stable Roche-lobe overflow (Istrate et al. 2016; Li et al. 2019). Most of the known objects of this type have been identified thanks to the mining of the Sloan Digital Sky Survey (SDSS) spectroscopic database (Gianninas et al. 2015; Bell et al. 2017; Brown et al. 2020b, 2022). With the advent of the astrometric and photometric data provided by the *Gaia* satellite (Gaia Collaboration 2018; Gaidos et al. 2023), many more ELM white dwarfs are being identified (Inight et al. 2021; Wang et al. 2022; Kosakowski et al. 2023a). We are currently in the process of building and characterising a volume-limited sample of ELM white dwarfs using *Gaia* plus follow-up spectroscopy (Pelisoli & Vos 2019). As a result of this endeavour, we have identified a peculiar ultra-short-period (<25 min) double white dwarf that presumably contains an ELM white dwarf, which we present and analyse in detail in this work.

The structure of the paper is as follows. In Sect. 2 we introduce J0526+5934, the target of our study. In Sect. 3 we describe our extensive follow-up campaign. The results, including our spectral and light curve analysis, are presented in Sect. 4. We discuss our results in Sect. 5 and summarise and conclude our work in Sect. 6.

2. J0526+5934

Pelisoli & Vos (2019) identified J0526+5934 (RA = 81.54342°, Dec = 59.57926°; *Gaia* DR3 ID = 282679289838317184) as an
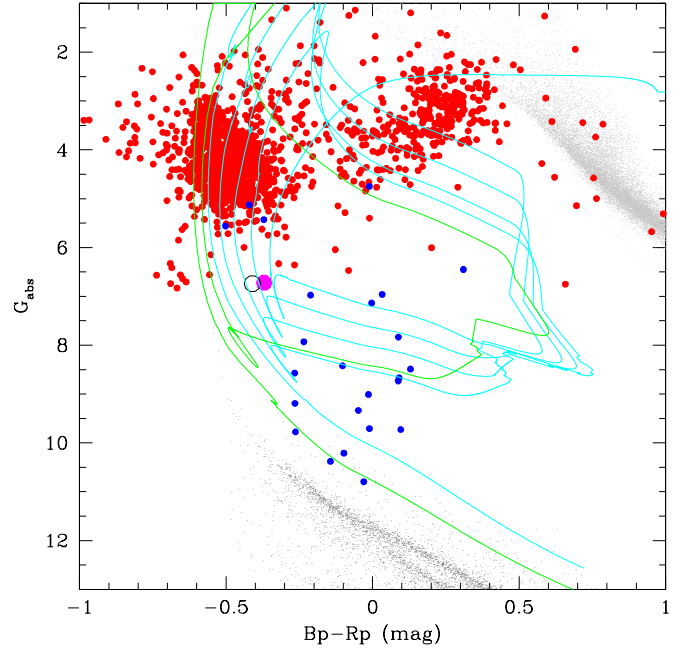
Fig. 2. Absolute magnitude–colour diagram of single white dwarfs (dark grey) and main sequence stars (light grey) within 100 pc from Jiménez-Esteban et al. (2023), hot sub-dwarf stars (red dots) from Geier (2020), and ELM white dwarfs (blue dots) from Brown et al. (2016), Kilic et al. (2017), and Pelisoli et al. (2018). J0526+5934 (solid magenta dot) falls in the transition region between hot sub-dwarf stars and ELM white dwarfs. The open black circle represents the $G_{\rm abs}$ vs. Bp-Rp that we obtain for J0526+5934 from our spectral modelling (Sect. 4.2), which is in good agreement with the *Gaia* observed value (magenta dot). All magnitudes have been de-reddened using the extinction provided by the Lallement et al. (2014) 3D maps except for J0526+5934 (in this case, we used the reddening obtained from our analysis; Sect. 4.2), and only objects with positive parallaxes and relative errors below 10% have been considered. The cyan and green lines represent the evolutionary tracks for a $0.226\,M_\odot$ and a $0.324\,M_\odot$ ELM white dwarf, respectively, from Istrate et al. (2016).

ELM white dwarf candidate. *Zwicky* Transient Facility (ZTF; Masci et al. 2019; Dekany et al. 2020), photometry is available for this object and our analysis of the g-band and r-band light curves indicated a very short period of $\simeq 10.25$ min (see Fig. 1). It is worth noting that the Scargle (1982) periodograms obtained from both datasets did not reveal any significant peak at double this value, which is, as we see in the next section, the true orbital period (Ren et al. 2023).

The location of J0526+5934 in the *Gaia* colour–magnitude diagram, as shown in Fig. 2, is far from that of the typical white dwarf locus, and within the region of hydrogen shell flashes of proto-ELM white dwarfs. As can be seen from the figure, J0526+5934 is also relatively close to the locus occupied by hot sub-dwarfs, and indeed it has been claimed by Kosakowski et al. (2023b) and Lin et al. (2024) that the visible component of this binary belongs to this category. This is mainly due to the fact that the authors measure a mass of $\simeq 0.36$–$0.38\,M_\odot$ for this compact object. In our analysis, we derive a mass for the visible component of $\simeq 0.26\,M_\odot$, which is fully compatible with the hypothesis that it is an ELM white dwarf. Although we find no robust evidence to rule out the sub-dwarf nature, we argue that the visible component of J0526+5934 is hence an ELM white dwarf and we treat it as such throughout the paper. We also assumed that the unseen companion is another white dwarf (although the possibility

exists that it belongs to a more exotic category such as a neutron star). Under these assumptions, J0526+5934 becomes the sixth ultra-short-period detached double white dwarf known to date, together with SDSS J065133.338+284423.37 (Brown et al. 2011, 12.7 min) ZTF J1539+5027 (6.9 min; Burdge et al. 2019a), PTF J0533+0209 (20.6 min; Burdge et al. 2019b; Chen et al. 2022), J232230.20+050942.06 (20 min; Brown et al. 2020a), and ZTF J2243+5242 (8.8 min; Burdge et al. 2020).

3. Observations

In this section we give details of the follow-up observations we carried out at the Telescopi *Joan Oró* (TJO), the Gran Telescopio Canarias (GTC), and the Thai National Telescope.

3.1. Telescopi Joan Oró

The orbital period of J0526+5934 is too short for obtaining a high signal-to-noise spectrum in one single exposure without avoiding orbital smearing, given that it is quite faint ($G = 17.5$ mag). For this reason, and with the aim of measuring an orbital period accurate enough to plan the spectroscopic observations, we first followed up on this object with the 0.8m TJO (Colomé et al. 2010) located in the Montsec Observatory in Lleida, Spain.

We used the Large Area Imager for Astronomy (LAIA) instrument equipped with the 4k × 4k Andor iKon XL CCD (charge-coupled device) and the Johnson-Cousins V filter. The observations took place on the night of 23 October 2020 and lasted for a total of ≃5 h. Individual exposure times were 130 s, reaching a signal-to-noise ratio of ≃50 for the target in each image. The readout time of the CCD is 8 s. The data were automatically reduced by the TJO internal pipeline, which also yields differential photometry for the target plus two comparison stars. The analysis of the TJO photometry resulted in an orbital period of 616.00 ± 0.66 s, in agreement with the ZTF measurement (Sect. 2; note that, in the same way as for the ZTF data, the strongest signal corresponded to half the true period).

3.2. Gran Telescopio Canarias

We obtained follow-up spectroscopy of J0526+5934 with the GTC at the Observatorio Roque de los Muchachos, La Palma. The telescope was equipped with the OSIRIS (Optical System for Imaging and low-Intermediate-Resolution Integrated Spectroscopy) instrument (Cepa et al. 2013), the 2000B grating and the 0.6″ slit. Thus, the spectra acquired covered the ≃3950–5700 Å wavelength range at a resolving power of ≃2100. The observations took place on 26 November 2022 and lasted ≃6.5 h.

Given the short orbital period of J0526+5934, we avoided exposures longer than 1 min; otherwise, the spectra would have suffered orbital smearing. We planned the observations under the assumption that the orbital period was the one we obtained from the analysis of the TJO data (Sect. 3.1). Thus, we aimed to obtain 37 cycles of 12 short exposures of $27.93 + t_{read}$ seconds (a total of 444 spectra), where t_{read} is the CCD readout time (23.4 s, including also the setup for the next exposure) and $27.93 = (P_{orb}/12) - t_{read}$, where P_{orb} is the expected orbital period. As a consequence, this strategy would allow us to take 37 spectra at each 1/12th of the orbit in 6.5 h, which we would then combine to obtain 12 spectra equally spread over the entire orbit. The orbital period uncertainty of ≃0.65 s (Sect. 3.1) implies a maximum drift of 24 s after the 6.5 h, assuming the orbital period was

616 s. Given that the total time of 51.33 s (27.93 s of exposure plus 23.4 s of readout time) is longer than the maximum drift, this implies the 37 spectra at each 1/12th taken over the 6.5 h can be combined without causing any smearing.

The observations were carried out following the above strategy, and we reduced and calibrated the spectra using the `pamela` (Marsh 1989) and `MOLLY`[1] packages, respectively. When combining the 37 spectra at each 1/12th of the orbit, we found the spectra displayed a double-lined profile of nearly identical lines. It was then that we realised these lines were exactly the same but shifted by the same amount both towards the blue and the red. In other words, the orbital period was twice the value we measured from the TJO data, 1232.00 ± 0.66 s, in agreement with the period reported by Ren et al. (2023), Kosakowski et al. (2023b), and Lin et al. (2024), and we were sampling 24 points in the orbit rather than 12. As a consequence, we then combined the spectra at each 1/24th of the orbit. That is, we obtained 24 spectra of J0526+5934 equally spread over the orbit.

We note that since the orbital period is double what we expected, the maximum drift drops to 12 s for the length of the observations. As a consequence, our spectra do not suffer from orbital smearing.

3.3. Thai National Telescope

More follow-up photometric data of J0526+5934 were obtained with the 2.4m Thai National Telescope in Doi Inthanon, Thailand, using the ULTRASPEC instrument (Dhillon et al. 2014). The observations were conducted on 29 March 2020, 10 December 2020, and 5 February 2021, when we followed up the target for 2× the orbit, 3× the orbit, and 8× the orbit on each respective night. We opted to use the $KG5$ filter ($u' + g' + r'$, Hardy et al. 2017) for all of our observations to optimise the signal-to-noise ratio. The data were taken in windowed mode with box sizes of ≃3–4 arcmin to ensure enough comparison stars within the field of view.

The data were then reduced using the HiPERCAM pipeline (Dhillon et al. 2007) to obtain the fluxes of J0526+5934 and nearby comparison stars. The signal-to-noise ratio from our data is 40 with 2.1 s exposure time during the first observing night. The sky was clear on 29 March 2020 with seeing between 2 and 2.5 arcsec. We obtained a signal-to-noise ≲30 in the second and the third runs due to weather conditions (intermittent clouds and seeing ≲1.5–3 arcsec). The exposure times used on both nights was ≃2 s.

4. Results

4.1. Radial velocities and radial velocity curve

To measure the radial velocities from the 24 GTC spectra (see Sect. 3.2), we first fitted the Hβ absorption lines with a single Gaussian profile. We used these values to correct the spectra from the orbital motion, which we combined and run a model spectral fit (see details in Sect. 4.2) to obtain a preliminary best-fit model spectrum. In a second step, we used the `MOLLY` software to cross-correlate the normalised best-fit model spectrum to the 24 observed GTC spectra (also normalised). The cross-correlation technique yielded similar but more precise radial velocity values than those obtained from the Gaussian fits. The

---

[1] Developed by Tom Marsh and available at https://cygnus.astro.warwick.ac.uk/phsaap/software/molly/html/INDEX.html.
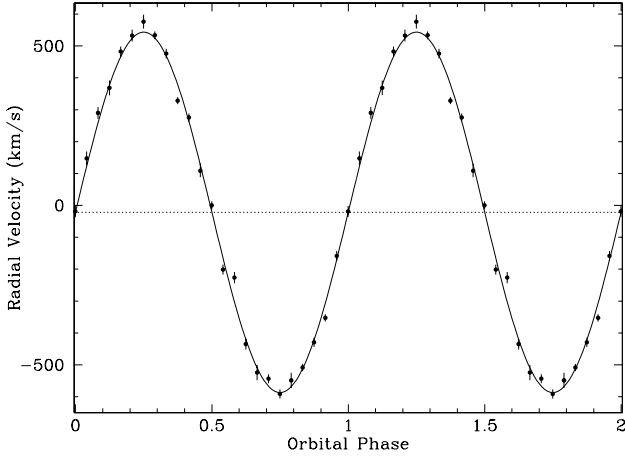
Fig. 3. Radial velocities of J0526+5934. The orbital motion of the ELM white dwarf is represented as a function of the orbital phase (solid dots). Phase 0 indicates the time of inferior conjunction. The solid line is the best sine fit to the data, and the horizontal dotted line indicates the systemic velocity.

observed spectra were then corrected from the orbital motion using these refined velocities and the combined spectrum was then re-fitted to derive the effective temperature and surface gravity of the ELM white dwarf (see details in Sect. 4.2).

Once the radial velocities were obtained using the above procedure, we represented them as a function of orbital phase and fitted them with a sine curve. The radial velocity curve and the corresponding sine fit can be seen in Fig. 3. From this fit we obtained a semi-amplitude velocity of $565.2 \pm 3.2 \, \mathrm{km \, s^{-1}}$ for the brightest component and a systemic velocity of $-21.6 \pm 2.2 \, \mathrm{km \, s^{-1}}$.

4.2. Spectral model fit and mass of the visible component

To measure the atmospheric parameters of the ELM white dwarf, we performed a simultaneous fit to our co-added GTC spectra (Sect. 3.2) and the available photometry (*Gaia* DR3 and Pan-STARRS DR1). The result can be seen in Fig. 4. For this purpose, we used the Koester 1D local thermodynamic equilibrium white dwarf model atmosphere code (Koester 2010), assuming a negligible contribution from the white dwarf companion (see Sect. 4.4). As free parameters, we fitted the effective temperature (T_{eff}), the surface gravity ($\log g$), the helium abundance ($\log(\mathrm{He/H})$), the solid angle of the star on the sky (Ω), the interstellar reddening ($E(B-V)$), and finally its rotational broadening ($v_{\mathrm{eq}} \sin i$; where v_{eq} is the rotational velocity at the equator and i is the inclination).

Our fit consisted of an iterative χ^2 minimisation against the spectrum and photometry. Rather than construct a grid of models around the approximate solution and interpolating, we recalculated our atmosphere code at each iteration in the fit, to ensure self-consistency. After computing the model at the start of each iteration, we convolved the model spectrum by an instrumental broadening of $R = 2165$, as expected for the R2000B grating. We then scaled the model to observational fluxes by multiplying by the solid angle, Ω. We then applied the input interstellar reddening to the model, and finally applied rotational broadening with a kernel determined from the Claret four-term limb-darkening law evaluated in the SDSS g band.

We calculated synthetic photometry in each of the observed bands, by integrating the model over each bandpass, to compare against the observed fluxes, where we assumed each flux contained an additional 0.01 mag systematic uncertainty. To compare with the spectral data, we normalised the model against the spectrum using a spline fit to their spectral ratio (in order to remove the effects of imperfect flux calibration). We determined the total χ^2 fit by adding the individual χ^2 for the spectrum and photometry. We also included the measured reddening $E(B-V) = 0.27 \pm 0.05$ from the 3D extinction maps of Lallement et al. (2014) as an additional data point in the total χ^2 effectively acting as a prior on our fitted reddening parameter.

After performing this minimisation, we found $T_{\mathrm{eff}} = 27\,330 \pm 370 \, \mathrm{K}$, $\log g = 6.213 \pm 0.050 \, \mathrm{dex(cm \, s^{-2})}$, $\log(\mathrm{He/H}) = -2.20 \pm 0.03 \, \mathrm{dex}$, $\Omega = (9.41 \pm 0.23) \times 10^{-24} \, \mathrm{sr}$, $E(B-V) = 0.383 \pm 0.007$, and $v_{\mathrm{eq}} \sin i = 299 \pm 10 \, \mathrm{km \, s^{-1}}$. All quoted uncertainties are determined from the covariance matrix of the best fit. From these we determined the stellar radius to be $R_{\mathrm{ELM}} = 0.065 \pm 0.005 \, R_\odot$, the ELM white dwarf mass to be $M_{\mathrm{ELM}} = 0.257 \pm 0.049 \, M_\odot$, and their Pearson correlation as $\rho = 0.785$. From the best fitting model spectrum, we determined the intrinsic *Gaia* absolute magnitude to be $G_{\mathrm{abs}} = 6.73 \pm 0.17 \, \mathrm{mag}$ (with the uncertainty considering the errors on Ω and the parallax) and its *Gaia* colour to be Bp-Rp $= -0.419 \pm 0.005$.

An important source of uncertainty in our fit is the degree of rotational broadening. Our radius and orbital period measurements (assuming tidal locking) suggest $v_{\mathrm{eq}} = 231 \pm 17 \, \mathrm{km \, s^{-1}}$, which is notably smaller than our measured value of $v_{\mathrm{eq}} \sin i$ (our light curve analysis in the following section indicates an inclination of 65 ± 7 degrees). While we cannot provide a definite explanation for this discrepancy, we acknowledge that our model of rotational broadening does not account for the ellipsoidal distortion of the star or gravity darkening, which will certainly lead to more complex broadening. Nevertheless, we do not believe this invalidates our other stellar parameters, as our measured $v_{\mathrm{eq}} \sin i$ simply represents the best fitting value with an incomplete model. If we adopt an alternative broadening profile such a rectangular distribution (which gives more weight to the most extreme Doppler shifts), we find a lower value of $v_{\mathrm{eq}} \sin i = 247 \pm 10 \, \mathrm{km \, s^{-1}}$, while the other parameters are virtually unchanged.

4.3. Light curve fit

The ULTRASPEC light curve shows sinusoidal variations on half the orbital period, indicating that we are seeing ellipsoidal modulation originating from the tidally distorted ELM white dwarf. We can use the amplitude of this variation to set constraints on the stellar and binary parameters since the fractional semi-amplitude is given by

$$\frac{\partial F}{F} = 0.15 \frac{(15 + u_1)(1 + \beta_1)}{3 - u_1} \left(\frac{R_1}{a}\right)^3 q \sin^2 i \qquad (1)$$

(Morris & Naftilan 1993; Zucker et al. 2007), where u_1 is the linear limb-darkening coefficient, β_1 is the gravity-darkening exponent, R_1/a is the radius scaled by the orbital separation, $q = M_2/M_1$ is the mass ratio and i is the inclination. The subscript 1 refers to the ELM white dwarf, while 2 refers to the white dwarf companion.

In the absence of any additional information when fitting the ellipsoidal modulation there is complete degeneracy between the mass ratio, scaled radius of the ELM white dwarf and inclination. Therefore, we use the constraints on the mass and radius of the ELM white dwarf (i.e. M_1 and R_1) from the spectral modelling to break some of this degeneracy, resulting in the
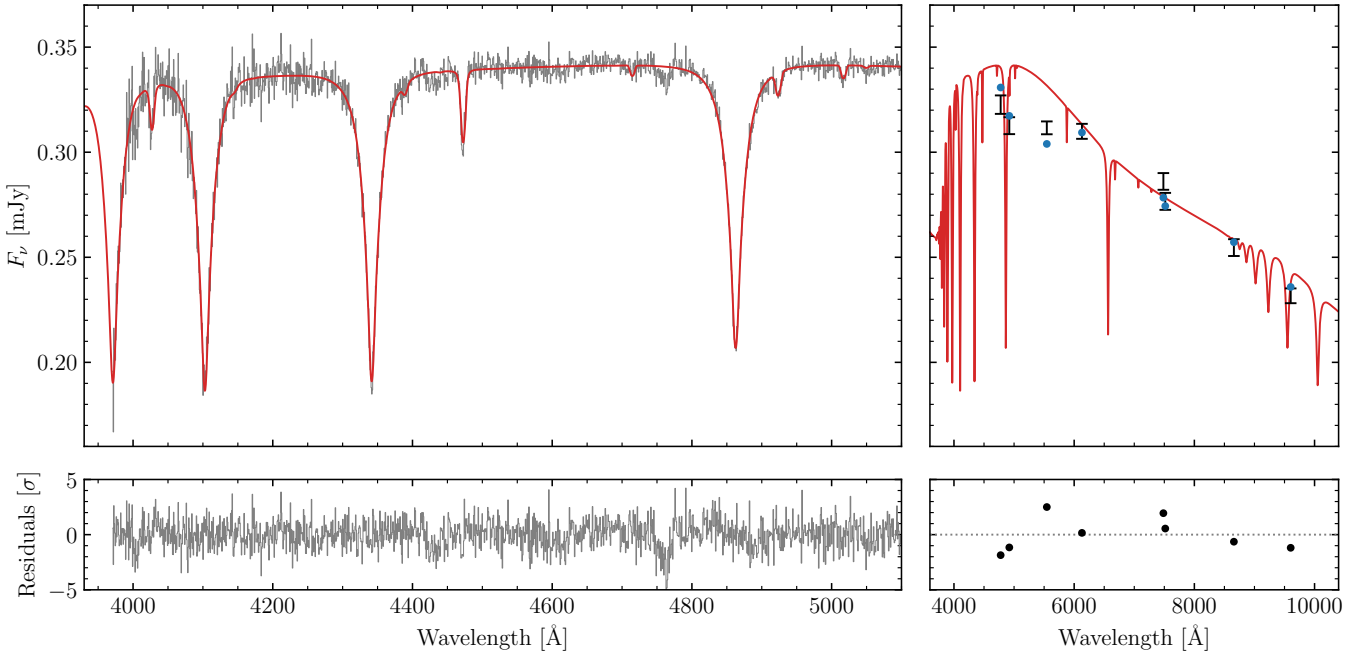
Fig. 4. Fit to the spectrum of J0526+5934 (left panels) with the residuals shown below. The best fitting model (red) includes the measured interstellar reddening. The spectral fluxes have been re-calibrated against the model with a spline fit to their ratio. While the GTC spectrum extends to 5700 Å, it is featureless beyond 5100 Å, and so those wavelengths are not shown. The same model is shown against the photometry (black error bars), with synthetic photometry shown by the blue points (right panels). Error bars include the assumed 0.01 mag systematic uncertainty. Again, their residuals are shown below.
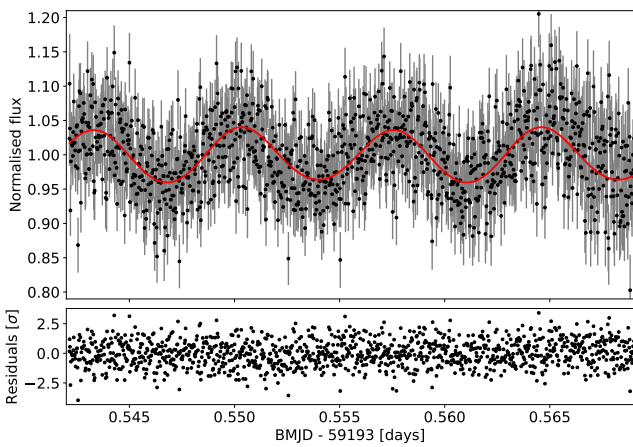
Fig. 5. ULTRASPEC $KG5$ band light curve with the best-fit model overplotted in red. The bottom panel shows the residuals to this fit in terms of standard deviations from the model.

ellipsoidal amplitude depending only on M_2 and i (since a is a function of M_1, M_2, and P_{orb}), essentially allowing us to place constraints on the mass of the unseen white dwarf companion from the light curve.

Rather than simply using Eq. (1) (which ignores any contribution from the companion or any irradiation effects and does not allow a more sophisticated treatment of limb darkening), we modelled the light curve in a more complete way using LCURVE (Copperwheat et al. 2010) and fitted the ULTRASPEC data using the Markov chain Monte Carlo (MCMC) method (Press et al. 2007), implemented using the Python package EMCEE (Foreman-Mackey et al. 2013). The fitted parameters were: the mass of the ELM white dwarf (M_1), the mass of the white dwarf companion (M_2), the radius of the ELM white dwarf (R_1), the inclination (i), the time of the superior conjunction of the ELM white dwarf (T_0) and the orbital period (P_{orb}). No limb-darkening coefficients or gravity-darkening exponents have been computed for the parameter space of the ELM white dwarf in the ULTRASPEC $KG5$ filter. Therefore, following the method in Claret et al. (2020), we created a small grid of limb-darkening (four-term law) and gravity-darkening values in the $KG5$ band for a white dwarf effective temperature of 27 000 K and a range of surface gravities between 6.0 and 6.5 in steps of 0.1 dex, using updated model DA spectra from Koester (2010)[2]. Then for a chosen value of M_1 and R_1 we computed the limb-darkening coefficient and gravity-darkening exponent of the ELM white dwarf by interpolating this grid. We fixed the temperature of the ELM white dwarf to the spectroscopically determined value of 27 330 K and also fixed the temperature of the white dwarf companion. Given that the companion contributes a negligible amount of flux to the ULTRASPEC light curve the choice of temperature is somewhat arbitrary. Nevertheless, to check that this parameter has no effect on the final results we fitted the light curve twice, once with the temperature of the companion fixed at 8000 K and again with it fixed at 20 000 K. We also fixed the radius of the companion to a typical white dwarf radius of 0.015 $R_\odot$. Again, this parameter makes little difference given the extreme flux ratio in the $KG5$ band.

We placed a multivariate Gaussian prior on M_1 and R_1 with a correlation value of $\rho_{MR} = 0.785$, based on the spectroscopi-

---

[2] Note that the dominant source of continuum opacity in the visible component of J0526+5934 is from hydrogen. The additional continuum opacity from the $\simeq$1% of He in the atmosphere is negligible. Indeed, limb- and gravity-darkening coefficients derived from a pure-hydrogen DA model (i.e. without He traces) of the same effective temperature and surface gravity as our best-fit model are nearly identical to those directly obtained from the best-fit model.
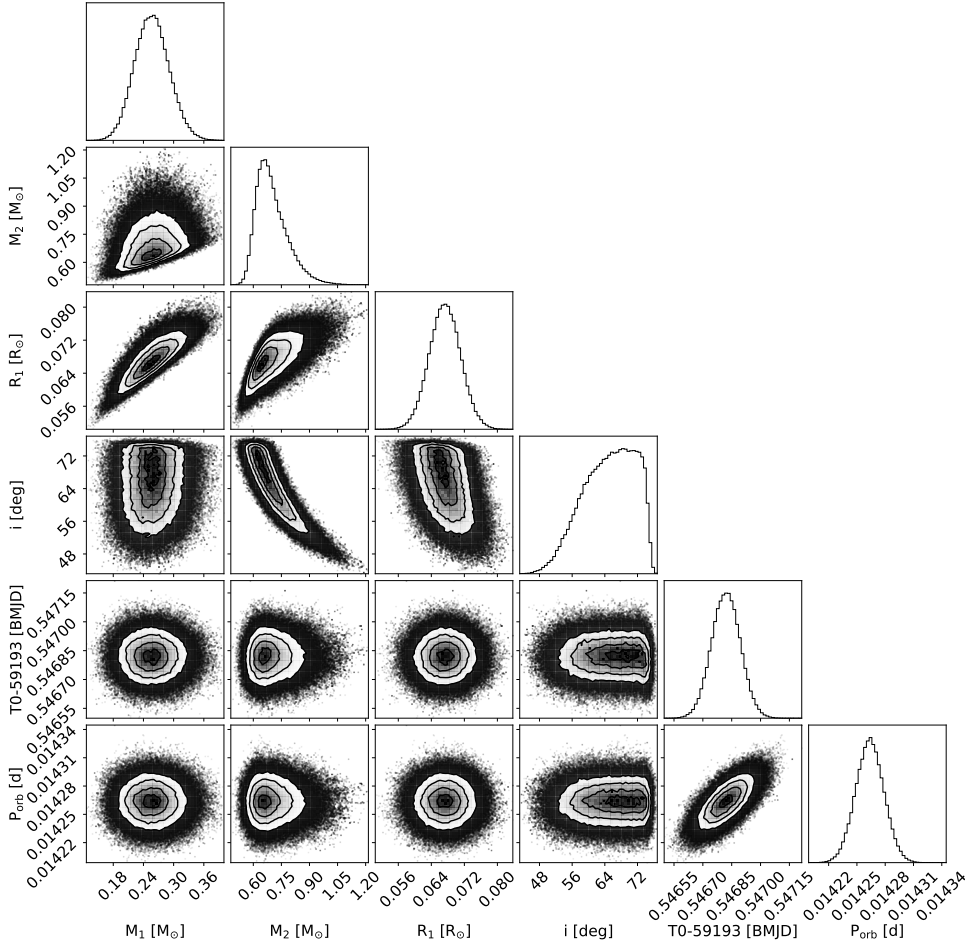
Fig. 6. Posterior probability distributions for model parameters obtained through fitting the ULTRASPEC *KG*5-band light curve. Grey scales and contours represent the joint probability distributions for each pair of parameters, while the histograms show the marginalised probability distributions for each parameter.

cally derived values, which takes into account the fact that these two parameters are strongly correlated. We placed a Gaussian prior on P_{orb} based on the TJO and GTC results and a uniform prior on the inclination between 1 and 90 degrees. We also used the radial velocity curve to determine which minimum in the light curve corresponded to the superior conjunction of the ELM white dwarf and placed a uniform prior on T_0 between the time of this minimum and $\pm 0.5\,P_{orb}$ to ensure that the fit did not try to jump to the next cycle. Finally, at each step in the fitting process we computed the radial velocity semi-amplitude of the ELM white dwarf (which is only a function of M_1, M_2, P_{orb}, and i) and compared this to the measured value via a Gaussian prior based on the measured value. This final constraint helps break some of the degeneracy between M_2 and i.

Our MCMC fitting used 50 walkers, each with 20 000 points. The first 5000 points were classed as 'burn-in' and were removed from the final results. The ULTRASPEC light curve and best-fit model is shown in Fig. 5, while the posterior probability distributions are shown in Fig. 6. As expected we found no difference in the results between an 8000 K and 20 000 K companion. We found that inclinations greater than around 75 degrees are excluded, since we would expect to see the ELM white dwarf eclipsed by its companion at these high inclinations (which is not seen in the light curve). Inclinations lower than around 40 degrees are also ruled out, since at these low inclinations it is not possible to generate a large enough ellipsoidal signal in the light curve while simultaneously being consistent with the measured radial velocity semi-amplitude of the ELM white dwarf. The best consistency is found at higher inclinations, and

hence lower companion white dwarf masses, as reflected in the marginalised probability distribution for M_2 in Fig. 6. Overall we constrain the inclination to 65 ± 7 degrees and the companion white dwarf mass to $0.71^{+0.09}_{-0.06}\,M_\odot$. This mass is consistent with our assumption that the unseen companion is a white dwarf. The distributions for P_{orb}, M_1 and R_1 are entirely driven by the priors placed on these values, while we find a value for T_0 of BMJD(TDB) = 59193.54682(7), where the number in the parenthesis represents the uncertainty on the final digit.

4.4. Effective temperature of the white dwarf companion

We attempted to obtain an upper limit to the white dwarf companion's effective temperature by determining by how much the synthetic spectrum of a (hydrogen-rich) white dwarf can be added to the spectrum of the ELM white dwarf without affecting the observed spectral features. To that end we considered the best-fit model to the observed GTC combined spectrum from Sect. 4.2 and subtracted model spectra from the Koester (2010) updated collection of any given effective temperature and surface gravity between 7.8 and 8.3 dex (that is a surface gravity that corresponds to a mass of $0.71^{+0.09}_{-0.06}\,M_\odot$, as derived from the light curve fit). After subtracting each white dwarf model, we measured the resulting Hβ equivalent width (EW). We assumed the spectral features to be different from those sampled by the best-fit model to the observed spectrum when the EW decreased by more than 25%. Fitting such spectra would result in stellar parameters different from those obtained in Sect. 4.2 due to the change in the Balmer line profiles. However, we found that the

Table 1. Orbital and stellar parameters for the visible component and the unseen companion of J0526+5934.

Binary	This work	Kosakowski et al. (2023b)	Lin et al. (2024)
Orbital period (s)	1232.00 ± 0.66	1230.37467 ± 0.00007	1230.374556 ± 0.000318
Orbital inclination (°)	65 ± 7	$57.1^{+4.3}_{-4.1}$	$68.2^{+3.7}_{-5.2}$
Systemic velocity (km s^{-1})	-21.6 ± 2.2	-40.7 ± 4.1	-35.6 ± 4.4
Visible component			
T_{eff} (K)	$27\,330 \pm 370$	$27\,300 \pm 260$	$25\,480 \pm 360$
$\log g$ (dex)	6.213 ± 0.050	6.37 ± 0.03	6.355 ± 0.068
$M(M_\odot)$	0.257 ± 0.049	$0.378^{+0.066}_{-0.060}$	$0.360^{+0.080}_{-0.071}$
$R(R_\odot)$	0.065 ± 0.005	0.070 ± 0.005	0.0661 ± 0.0054
[He/H] (dex)	-2.20 ± 0.03	-2.45 ± 0.06	-2.305 ± 0.062
K (km s^{-1})	565.2 ± 3.2	558.3 ± 4.8	$559.6^{+6.4}_{-6.5}$
Unseen WD			
$M(M_\odot)$	$0.71^{+0.09}_{-0.06}$	$0.887^{+0.110}_{-0.098}$	$0.735^{+0.075}_{-0.069}$
T_{eff} (K)	<6700	–	–

Notes. We include the values measured by Kosakowski et al. (2023b) and Lin et al. (2024) for comparison.

EW remain unaltered in all cases, with the ELM contribution to the total flux always being larger than 96%. This implied no constraint on the unseen white dwarf companion's effective temperature could be placed with this exercise. More stringent constraints on this value are discussed in Sect. 5.

4.5. Comparison to Kosakowski et al. (2023b) and Lin et al. (2024)

The most relevant orbital and stellar parameters we have obtained in this section for J0526+5934 are provided in Table 1. Most of our measured values are similar to those recently obtained by Kosakowski et al. (2023b) and Lin et al. (2024), although slight differences arise (see Table 1). The most important difference in the context of this paper is that we derive a lower surface gravity for the visible component and, as a consequence, a lower mass. In the three studies, these values are directly obtained from the spectral fitting analysis. Whilst our observational strategy ensured that our results are not affected by orbital smearing (Sect. 4.1), the exposure times used during the spectroscopic observations performed by Kosakowski et al. (2023b) covered ≃10% of the orbit; therefore, their combined spectrum was considerably affected by smearing. The observations carried out by Lin et al. (2024) were clearly affected by this effect too. Although the authors fitted all their spectra simultaneously to account for this, our results should yield more accurate values simply because orbital smearing is efficiently taken into account. As a consequence, our derived mass provides robust evidence that the visible component in J0526+5934 is not a hot sub-dwarf star but rather an ELM white dwarf, as we have been assuming in this paper. In the following section we discuss this hypothesis in detail.

5. Discussion

The deduced stellar mass values for the bright component of J0526+5934 strongly reduce the likelihood of it being a hot sub-dwarf star. In fact, the minimum mass requirement for a sub-dwarf star typically stands at approximately $0.30\,M_\odot$ (Arancibia-Rojas et al. 2024). In particular, detailed calculations by Han et al. (2003) predict this minimum mass to be about $0.33\,M_\odot$. This is due to the fact that stars below this mass threshold are unable to initiate core-helium burning within their cores

under non-degenerate conditions. From the observational point of view, the mass distribution of hot sub-dwarf stars has been found to range between ≃$0.3\,M_\odot$ and $0.63\,M_\odot$, with a clear peak at ≃$0.45\,M_\odot$ and very few objects below ≃$0.3\,M_\odot$ (Fontaine et al. 2012; Schaffenroth et al. 2022; Lei et al. 2023). This gives further support to our hypothesis that the visible component of J0526+5934 is an ELM white dwarf.

ELM white dwarfs are expected to originate from unstable mass loss through the common-envelope ejection channel and the stable Roche lobe overflow channel, as discussed recently by Li et al. (2019). Existing evolutionary tracks for ELM white dwarfs are based on the assumption of stable Roche lobe overflow, involving stable mass transfer (see Althaus et al. 2013; Istrate et al. 2016 and references therein). Consequently, ELM white dwarf evolutionary models derived under this framework are characterised by an upper limit on the possible H-layer thickness that a given-mass ELM white dwarf model can possess. This implies that residual stable hydrogen burning emerges as the primary energy source during the cooling phase of the white dwarf, leading to the occurrence of multiple hydrogen flashes at the onset of the cooling track.

The manifestation of hydrogen flashes results in diverse potential solutions for the observed ELM white dwarf component. Specifically, from the evolutionary sequences computed by Althaus et al. (2013), we deduced a stellar mass of $0.237 \pm 0.035\,M_\odot$, a radius of $0.06 \pm 0.006\,R_\odot$, a cooling age of 260 ± 240 Myr, and a helium surface abundance [He/H] in the range of -2. and -4. These values perfectly agree with the observational inferences for the J0526+5934 bright component (Sect. 4.2), strong evidence that the visible object is an ELM white dwarf. In particular, the derived mass value is in agreement with the predictions of population property studies of ELM white dwarfs in double degenerate systems, which suggests that intrinsic masses for ELM white dwarfs peak around $0.25\,M_\odot$ for the CE channel (Li et al. 2019). The considerable range in derived cooling ages are the result of residual hydrogen burning in the envelope.

It is noteworthy that the helium abundance predicted by cooling sequences is also in agreement with our independent value obtained from the spectral analysis performed in Sect. 4.2. Gravitational settling rapidly depletes metals in the atmospheres of white dwarfs; however, due to the lower surface gravities characterising ELM white dwarfs, the impact of gravitational settling

is less pronounced. This explains that traces of helium persist in the envelope at the effective temperature of the ELM component. For low-mass ELM white dwarfs, a pure hydrogen envelope is expected, albeit at significantly lower effective temperatures. The helium abundances predicted by the cooling sequences of Althaus et al. (2013) are likely a conservative lower limit. Higher helium abundances could potentially be expected due to rotational mixing, countering the effects of gravitational settling in the surface layers of young ELM proto-white dwarfs. However, as the ELM contracts and embarks on its cooling track, the efficiency of rotational mixing diminishes, and the role of rotation in augmenting helium abundance becomes less significant, as discussed by Istrate et al. (2016).

The formation of ELM white dwarfs with hydrogen contents lower than expected from stable Roche lobe overflow cannot be ruled out. Specifically, Strickler et al. (2009) concluded that the presence of a population of low-mass He-core white dwarfs with thin hydrogen envelopes in NGC 6397 cannot be discarded. More recently, Irrgang et al. (2021) demonstrated the necessity of a thin H envelope in J1604+1000, a proto-ELM white dwarf weighing approximately 0.21 $M_\odot$ likely resulting from a common-envelope event. Moreover, a comparative analysis of the mass distribution of observed ELM white dwarfs with theoretical expectations by Li et al. (2019) has suggested that the ELM white dwarfs arising from the common-envelope channel could be characterised by thinner H envelope compared to those resulting from stable Roche lobe channel. Finally, asteroseismological analysis support the presence of thin H envelopes (1–2 order of magnitude thinner than predicted by the stable Roche lobe overflow channel) in certain pulsating ELM white dwarfs (Calcaferro et al. 2018b).

While the majority of ELM white dwarfs are discovered in double white dwarf systems resulting from common-envelope episodes, nearly all evolutionary calculations that involve stable mass transfer are applied to derive the properties of the white dwarf components in such systems. However, it could be expected that in ELM white dwarfs resulting from the common envelope, the recurrent hydrogen shell flashes may not occur, because of the minor role of residual H burning. In fact, the evolution of proto-ELM white dwarfs depends on the mass of the hydrogen-rich layer above the helium core, which is determined by the detailed common-envelope ejection process, the most uncertain phase in binary evolution (Li et al. 2019). A reduction in the thickness of the hydrogen envelope by a factor of 2 causes residual hydrogen burning to become negligible (Calcaferro et al. 2018a). With these considerations in mind (i.e. neglecting the occurrence of hydrogen flashes), we should expect a stellar mass of approximately 0.27 $M_\odot$, also in agreement with the observational inference. The resulting cooling times are expected to be much shorter than the cooling times of their counterpart with thick hydrogen envelope (see Calcaferro et al. 2018a).

From the observational data of J0526+5934 and based on the probable initial configuration of the system and cooling times, we can infer an upper limit on the effective temperature of the unseen white dwarf companion. According to Li et al. (2019), the most likely progenitors of ELM white dwarfs from the common-envelope channel have masses in the range 0.95–1.25 $M_\odot$. Given that the common-envelope channel is responsible for ELM white dwarfs in double degenerate systems with a helium-core white dwarf more massive than about 0.22 $M_\odot$ (Li et al. 2019), we adopt a value of 1.25 $M_\odot$ as the maximum stellar mass for the progenitor of the ELM component. This would yield an age of approximately 3.8 Gyr for the progenitor

to leave the main sequence (Miller Bertolami 2016). Considering the potential mass range for the unseen white dwarf companion (Table 1), the minimum mass of its progenitor would be of the order of 3.0 $M_\odot$, suggesting a main sequence lifetime of 0.3 Gyr (Miller Bertolami 2016). Thus, the newly formed white dwarf should have been undergoing cooling for at least 3.5 Gyr. During this period, and depending on its mass, the invisible white dwarf component should have attained an effective temperature within the range of 5700–6700 K. These inferred values serve as upper limits considering that the ELM could have arisen from a progenitor less massive than 1.25 $M_\odot$.

By considering J0526+5934 as a compact binary star composed of two white dwarfs of masses of 0.26 $M_\odot$ and 0.71 $M_\odot$ (Table 1), we estimate the merger time due to the emission of gravitational waves (τ; in Myr) from the following expression:

$$\tau = 47925 \frac{(M_1 + M_2)^{1/3}}{M_1 M_2} P^{8/3}, \qquad (2)$$

where P is the orbital period in days and the masses are in units of $M_\odot$ (Kraft et al. 1962). This results in just $\simeq 3$ Myr. The result of the merger, assuming no mass loss takes place during the process, would be a massive ($\simeq 1 M_\odot$) white dwarf. A relatively large percentage of such massive white dwarfs is expected to arise from this kind of merger (Cheng et al. 2019; Temmink et al. 2020; Kilic et al. 2023), which can partially explain the high-mass excess observed in the white dwarf mass distributions over the last years (Rebassa-Mansergas et al. 2015a,b; Jiménez-Esteban et al. 2023; Kilic et al. 2020). It is also possible that the system ends up as a type Ia supernova. As indicated by Shen (2015), in this scenario the ELM white dwarf would begin transferring material (sufficiently enriched in He) and a He detonation would occur during the subsequent merger of the two white dwarfs, thus producing a type Ia supernova.

6. Summary and conclusions

We have presented an independent observational and theoretical study of the ultra-short-period binary J0526+5934. The observations were carried out at the TJO, the GTC, and the Thai National Telescope, and the evolutionary models employed were those from the La Plata group. We have provided constraints on the orbital and stellar parameters of both stellar components. Most of our results are similar to those obtained by the previous analyses of Kosakowski et al. (2023b) and Lin et al. (2024). However, we find a mass for the visible component of $0.26 \pm 0.05\,M_\odot$ (from the observational analysis) or $0.237 \pm 0.035\,M_\odot$ (from the theoretical evolutionary tracks). This is lower than the reported values of $0.378^{+0.066}_{-0.060}\,M_\odot$ from Kosakowski et al. (2023b) and $0.360^{+0.080}_{-0.071}\,M_\odot$ from Lin et al. (2024). This difference is key when interpreting the nature of the visible component. Whilst the results of Kosakowski et al. (2023b) and Lin et al. (2024) favour a hot sub-dwarf star, our analysis is much more in agreement with an ELM white dwarf. However, these three studies cannot completely rule out the alternative scenario, and future observations may shed further light on this remarkable object. For instance, forthcoming extremely large-aperture telescopes equipped with high-resolution spectrographs will allow high signal-to-noise ratio spectra with short exposures to be acquired, and a better determination of radial velocities.

References

Althaus, L. G., Córsico, A. H., Isern, J., & García-Berro, E. 2010, A&A Rev., 18, 471

Althaus, L. G., Miller Bertolami, M. M., & Córsico, A. H. 2013, A&A, 557, A19

Arancibia-Rojas, E., Zorotovic, M., Vučković, M., et al. 2024, MNRAS, 527, 11184

Bauer, E. B., Schwab, J., Bildsten, L., & Cheng, S. 2020, ApJ, 902, 93

Bell, K. J., Gianninas, A., Hermes, J. J., et al. 2017, ApJ, 835, 180

Blouin, S., Dufour, P., Thibeault, C., & Allard, N. F. 2019, ApJ, 878, 63

Breedt, E., Steeghs, D., Marsh, T. R., et al. 2017, MNRAS, 468, 2910

Brown, W. R., Kilic, M., Hermes, J. J., et al. 2011, ApJ, 737, L23

Brown, W. R., Gianninas, A., Kilic, M., Kenyon, S. J., & Allende Prieto, C. 2016, ApJ, 818, 155

Brown, W. R., Kilic, M., Bédard, A., Kosakowski, A., & Bergeron, P. 2020a, ApJ, 892, L35

Brown, W. R., Kilic, M., Kosakowski, A., et al. 2020b, ApJ, 889, 49

Brown, W. R., Kilic, M., Kosakowski, A., & Gianninas, A. 2022, ApJ, 933, 94

Burdge, K. B., Coughlin, M. W., Fuller, J., et al. 2019a, Nature, 571, 528

Burdge, K. B., Fuller, J., Phinney, E. S., et al. 2019b, ApJ, 886, L12

Burdge, K. B., Coughlin, M. W., Fuller, J., et al. 2020, ApJ, 905, L7

Calcaferro, L. M., Althaus, L. G., & Córsico, A. H. 2018a, A&A, 614, A49

Calcaferro, L. M., Córsico, A. H., Althaus, L. G., Romero, A. D., & Kepler, S. O. 2018b, A&A, 620, A196

Camacho, J., Torres, S., García-Berro, E., et al. 2014, A&A, 566, A86

Camisassa, M. E., Althaus, L. G., Córsico, A. H., et al. 2016, ApJ, 823, 158

Camisassa, M. E., Althaus, L. G., Córsico, A. H., et al. 2019, A&A, 625, A87

Camisassa, M., Torres, S., Hollands, M., et al. 2023, A&A, 674, A213

Cepa, J., Bongiovanni, A., Pérez García, A. M., et al. 2013, in Highlights of Spanish Astrophysics VII, eds. J. C. Guirado, L. M. Lara, V. Quilis, & J. Gorgas, 868

Chen, H.-L., Tauris, T. M., Chen, X., & Han, Z. 2022, ApJ, 925, 89

Cheng, S., Cummings, J. D., & Ménard, B. 2019, ApJ, 886, 100

Claret, A., Cukanovaite, E., Burdge, K., et al. 2020, A&A, 634, A93

Cojocaru, R., Rebassa-Mansergas, A., Torres, S., & García-Berro, E. 2017, MNRAS, 470, 1442

Colomé, J., Casteels, K., Ribas, I., & Francisco, X. 2010, in Software and Cyberinfrastructure for Astronomy, eds. N. M. Radziwill, & A. Bridger, SPIE Conf. Ser., 7740, 77403K

Copperwheat, C. M., Marsh, T. R., Dhillon, V. S., et al. 2010, MNRAS, 402, 1824

Dekany, R., Smith, R. M., Riddle, R., et al. 2020, PASP, 132, 038001

Dhillon, V. S., Marsh, T. R., Stevenson, M. J., et al. 2007, MNRAS, 378, 825

Dhillon, V. S., Marsh, T. R., Atkinson, D. C., et al. 2014, MNRAS, 444, 4009

Fontaine, G., Brassard, P., Charpinet, S., et al. 2012, A&A, 539, A12

Foreman-Mackey, D., Hogg, D. W., Lang, D., & Goodman, J. 2013, PASP, 125, 306

Gaia Collaboration (Brown, A. G. A., et al.) 2018, A&A, 616, A1

Gaidos, E., Claytor, Z., Dungee, R., Ali, A., & Feiden, G. A. 2023, MNRAS, 520, 5283

Garcia-Berro, E., Hernanz, M., Isern, J., & Mochkovitch, R. 1988, Nature, 333, 642

García-Berro, E., Torres, S., Althaus, L. G., et al. 2010, Nature, 465, 194

Ge, H., Webbink, R. F., Chen, X., & Han, Z. 2015, ApJ, 812, 40

Geier, S. 2020, A&A, 635, A193

Gianninas, A., Kilic, M., Brown, W. R., Canton, P., & Kenyon, S. J. 2015, ApJ, 812, 167

Hallakoun, N., Maoz, D., Kilic, M., et al. 2016, MNRAS, 458, 845

Han, Z., Podsiadlowski, P., Maxted, P. F. L., & Marsh, T. R. 2003, MNRAS, 341, 669

Hardy, L. K., McAllister, M. J., Dhillon, V. S., et al. 2017, MNRAS, 465, 4968

Hollands, M. A., Tremblay, P. E., Gänsicke, B. T., Gentile-Fusillo, N. P., & Toonen, S. 2018, MNRAS, 480, 3942

Iben, I., & J. & Tutukov, A. V., 1984, ApJS, 54, 335

Inight, K., Gänsicke, B. T., Breedt, E., et al. 2021, MNRAS, 504, 2420

Irrgang, A., Geier, S., Heber, U., et al. 2021, A&A, 650, A102

Istrate, A. G., Marchant, P., Tauris, T. M., et al. 2016, A&A, 595, A35

Jeffery, E. J., von Hippel, T., DeGennaro, S., et al. 2011, ApJ, 730, 35

Jiménez-Esteban, F. M., Torres, S., Rebassa-Mansergas, A., et al. 2023, MNRAS, 518, 5106

Keller, P. M., Breedt, E., Hodgkin, S., et al. 2022, MNRAS, 509, 4171

Kilic, M., Brown, W. R., Gianninas, A., et al. 2017, MNRAS, 471, 4218

Kilic, M., Bergeron, P., Kosakowski, A., et al. 2020, ApJ, 898, 84

Kilic, M., Moss, A. G., Kosakowski, A., et al. 2023, MNRAS, 518, 2341

Koester, D. 2010, Mem. Soc. Astron. Ital., 81, 921

Korol, V., Koop, O., & Rossi, E. M. 2018, ApJ, 866, L20

Kosakowski, A., Kilic, M., Brown, W. R., Bergeron, P., & Kupfer, T. 2022, MNRAS, 516, 720

Kosakowski, A., Brown, W. R., Kilic, M., et al. 2023a, ApJ, 950, 141

Kosakowski, A., Kupfer, T., Bergeron, P., & Littenberg, T. B. 2023b, ApJ, 959, 114

Kraft, R. P., Mathews, J., & Greenstein, J. L. 1962, ApJ, 136, 312

Lallement, R., Vergely, J. L., Valette, B., et al. 2014, A&A, 561, A91

Lei, Z., He, R., Németh, P., et al. 2023, ApJ, 953, 122

Li, Z., Chen, X., Chen, H.-L., & Han, Z. 2019, ApJ, 871, 148

Lin, J., Wu, C., Xiong, H., et al. 2024, Nat. Astron., 8, 491

Liu, D., Wang, B., & Han, Z. 2018, MNRAS, 473, 5352

Maoz, D., Hallakoun, N., & Badenes, C. 2018, MNRAS, 476, 2584

Marsh, T. R. 1989, PASP, 101, 1032

Masci, F. J., Laher, R. R., Rusholme, B., et al. 2019, PASP, 131, 018003

McCleery, J., Tremblay, P.-E., Gentile Fusillo, N. P., et al. 2020, MNRAS, 499, 1890

Miller Bertolami, M. M. 2016, A&A, 588, A25

Morgan, D. P., West, A. A., Garcés, A., et al. 2012, AJ, 144, 93

Morris, S. L., & Naftilan, S. A. 1993, ApJ, 419, 344

Munday, J., Tremblay, P. E., Hermes, J. J., et al. 2023, MNRAS, 525, 1814

Napiwotzki, R., Karl, C. A., Lisker, T., et al. 2020, A&A, 638, A131

Nelemans, G., & Tout, C. A. 2005, MNRAS, 356, 753

O'Brien, M. W., Tremblay, P. E., Klein, B. L., et al. 2024, MNRAS, 527, 8687

Oswalt, T. D., Smith, J. A., Wood, M. A., & Hintzen, P. 1996, Nature, 382, 692

Parsons, S. G., Gänsicke, B. T., Marsh, T. R., et al. 2017, MNRAS, 470, 4473

Parsons, S. G., Gänsicke, B. T., Marsh, T. R., et al. 2018, MNRAS, 481, 1083

Parsons, S. G., Brown, A. J., Littlefair, S. P., et al. 2020, Nat. Astron., 4, 690

Pelisoli, I., & Vos, J. 2019, MNRAS, 488, 2892

Pelisoli, I., Kepler, S. O., Koester, D., et al. 2018, MNRAS, 478, 867

Press, W. H., Teukolsky, S. A., Vetterling, W. T., & Flannery, B. P. 2007, Numerical Recipes. The Art of Scientific Computing, 3rd edn. (Cambridge: University Press)

Raddi, R., Torres, S., Rebassa-Mansergas, A., et al. 2022, A&A, 658, A22

Rebassa-Mansergas, A., Schreiber, M. R., & Gänsicke, B. T. 2013, MNRAS, 429, 3570

Rebassa-Mansergas, A., Liu, X. W., Cojocaru, R., et al. 2015a, MNRAS, 450, 743

Rebassa-Mansergas, A., Rybicka, M., Liu, X. W., Han, Z., & García-Berro, E. 2015b, MNRAS, 452, 1637

Rebassa-Mansergas, A., Anguiano, B., García-Berro, E., et al. 2016, MNRAS, 463, 1137

Rebassa-Mansergas, A., Parsons, S. G., García-Berro, E., et al. 2017, MNRAS, 466, 1575

Rebassa-Mansergas, A., Parsons, S. G., Dhillon, V. S., et al. 2019a, Nat. Astron., 3, 553

Rebassa-Mansergas, A., Toonen, S., Korol, V., & Torres, S. 2019b, MNRAS, 482, 3656

Rebassa-Mansergas, A., Maldonado, J., Raddi, R., et al. 2021, MNRAS, 505, 3165

Rebassa-Mansergas, A., Maldonado, J., Raddi, R., et al. 2023, MNRAS, 526, 4787

Ren, L., Li, C., Ma, B., et al. 2023, ApJS, 264, 39

Scargle, J. D. 1982, ApJ, 263, 835

Schaffenroth, V., Pelisoli, I., Barlow, B. N., Geier, S., & Kupfer, T. 2022, A&A, 666, A182

Schreiber, M. R., Gänsicke, B. T., Rebassa-Mansergas, A., et al. 2010, A&A, 513, L7

Schreiber, M. R., Belloni, D., Zorotovic, M., et al. 2022, MNRAS, 513, 3090

Shen, K. J. 2015, ApJ, 805, L6

Skinner, J. N., Morgan, D. P., West, A. A., Lépine, S., & Thorstensen J. R. 2017, AJ, 154, 118

Strickler, R. R., Cool, A. M., Anderson, J., et al. 2009, ApJ, 699, 40

Temmink, K. D., Toonen, S., Zapartas, E., Justham, S., & Gänsicke, B. T. 2020, A&A, 636, A31

Torres, S., García-Berro, E., Althaus, L. G., & Camisassa, M. E. 2015, A&A, 581, A90

Torres, S., Rebassa-Mansergas, A., Camisassa, M. E., & Raddi, R. 2021, MNRAS, 502, 1753

van der Sluys, M. V., Verbunt, F., & Pols, O. R. 2006, A&A, 460, 209

van Roestel, J., Kupfer, T., Bell, K. J., et al. 2021, ApJ, 919, L26

Wang, K., Németh, P., Luo, Y., et al. 2022, ApJ, 936, 5

Webbink, R. F. 2008, in Astrophys. Space Sci. Lib., eds. E. F. Milone, D. A. Leahy, & D. W. Hobill, 352, 233

Whelan, J., Iben, Icko, & J., 1973, ApJ, 186, 1007

Woods, T. E., Ivanova, N., van der Sluys, M. V., & Chaichenets, S. 2012, ApJ, 744, 12

Zorotovic, M., & Schreiber, M. 2022, MNRAS, 513, 3587

Zorotovic, M., Schreiber, M. R., Parsons, S. G., et al. 2016, MNRAS, 457, 3867

Zucker, S., Mazeh, T., & Alexander, T. 2007, ApJ, 670, 1326